Supplementary Information for

Towards non-blinking and photostable perovskite quantum dots

Chenjia Mi[1], Gavin C. Gee[1], Chance W. Lander[1], Donghoon Shin[2], Matthew L. Atteberry[1], Novruz G. Akhmedov[1], Lamia Hidayatova[1], Jesse D. DiCenso[1], Wai Tak Yip[1], Bin Chen[2], Yihan Shao[1], Yitong Dong[1,3]*

[1]*Department of Chemistry and Biochemistry, The University of Oklahoma, Norman, Oklahoma 73019, USA.*

[2]*Department of Chemistry, Northwestern University, Evanston, Illinois 60208, USA.*

[3]*Center for Quantum Research and Technology, The University of Oklahoma, Norman, Oklahoma 73019, USA.*

Email: Yitong.Dong-1@ou.edu

Table of Contents:

Section 1: Demonstration of size-dependent defect tolerance of $CsPbBr_3$ QDs

Supplementary Note 1: Measuring the blinking behaviours of single $CsPbBr_3$ QDs

Four $CsPbBr_3$ QDs, with their sizes ranging from weak to strong confinement regimes, were passivated by NBA + PEA ligands (1:3, mass ratio) using the same solid-state ligand exchange approach. Incorporating NBA will interfere with PEA stacking and lead to insufficient surface passivation. Although passivated by identical ligand combinations, weakly confined QDs can better tolerate the under-passivated surface (Supplementary Fig. 1).

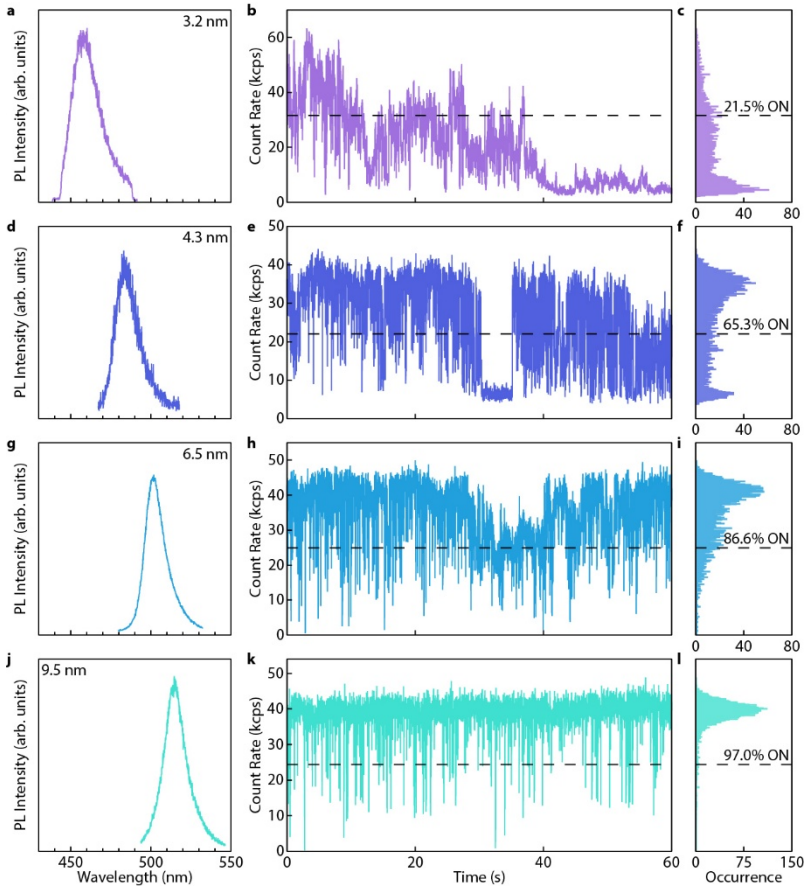

Supplementary Fig. 1 | Size-dependent defect tolerance of $CsPbBr_3$ QDs. a, d, g, j, Single QD PL spectrum of four $CsPbBr_3$ QDs passivated by a mixture of PEABr and NBABr (3:1 mass ratio). **b, e, h, k,** PL blinking traces of the four QDs with a bin time of 10 ms ($\langle N \rangle \sim 0.1$). **c, f, I, l,** The corresponding intensity distribution histograms.

Section 2: DFT modelling

Supplementary Note 2: Detailed methods used for DFT modelling

The ligand binding energies were calculated at the DFT level of theory using the projector augmented plane wave basis as implemented in the VASP 5.4 software package.[1, 2] Structures were optimized using the PBE functional[3] with D3(BJ)[4, 5] dispersion and dampening and an energy cutoff of 400 eV. Coordinates for the CsPbBr3 surfaces were obtained from the Crystallography Open Database (COD ID: 4510745).[6, 7] Charge neutral 2×2×1 surfaces were constructed with ASE.[8] A 4×4×1 Monkhorst–Pack grid was used for Brillouin zone sampling. All structures were optimized using the RMM-DIIS algorithm[9] with a self-consistent field (SCF) convergence criterion of 1×10^{-6} eV and an ionic convergence criterion of 1×10^{-3} eV. The coordinates of the perovskite atoms were fixed during optimization.

PEABr crystal structure and coordinates were obtained from a reported file in the database.[10] The phenyl rings in the crystal exhibit a high degree of π-π stacking.

Supplementary Note 3: Surface ligand configurations used in the DFT calculation

The energy of PEA or truncated DDA covered 2×2×1 (100) $CsPbBr_3$ slabs were calculated as a function of ligand numbers. The ligand binding energies were estimated by putting only one ligand on the slab (Supplementary Fig. 1, all other 7 sites are filled with Cs^+ to maintain charge neutrality). The resultant binding energy of 2.37 eV (for DDA) and 2.00 eV (for PEA) are comparable to that of similar compounds reported in other works. [11, 12]

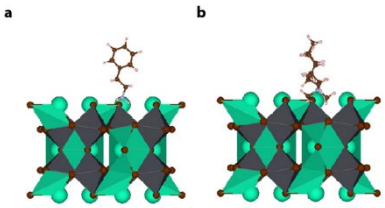

Supplementary Fig. 2 | The $CsPbBr_3$ slabs with a single bonded ligand. a, PEA and **b,** truncated DDA. The other surface sites were filled by Cs^+.

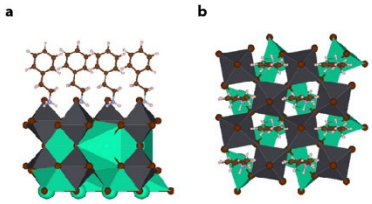

Supplementary Fig. 3 | The $CsPbBr_3$ slab with its surface fully covered by PEA. a, Side-view. **b,** Top-view.

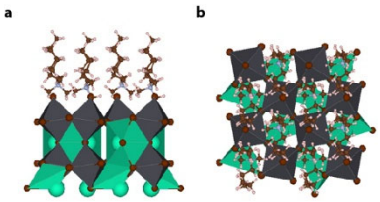

Supplementary Fig. 4 | The $CsPbBr_3$ slab with its surface fully covered by truncated DDA. a, Side-view. **b,** Top-view.

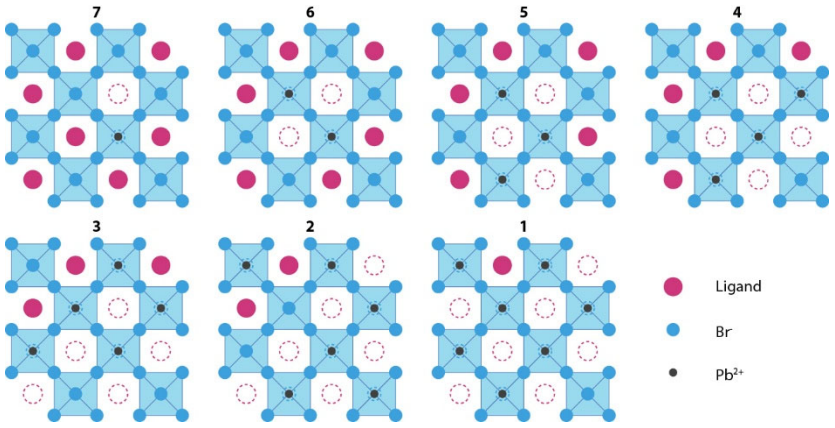

Supplementary Fig. 5 | Schemes of the surface ligand configurations for the PEA-covered $CsPbBr_3$ slabs. Dashed hollow circles represent vacant sites. PEA^+ and Br^- was removed together when reducing ligand coverage.

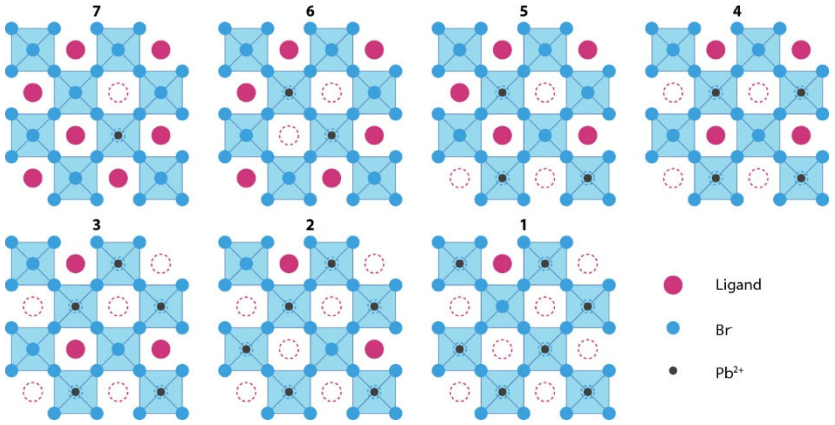

Supplementary Fig. 6 | Schemes of surface ligand configurations for the truncated DDA-covered $CsPbBr_3$ slabs. Dashed hollow circles represent vacant sites. DDA^+ and Br^- were removed together when reducing ligand coverage.

Supplementary Note 4: Entropy considerations

The above calculations yielded surface enthalpies. Entropy contributions from the structurally distinct DDA and PEA should be included for calculating the free energy of the system. The entropy difference between bound (solid-state) and free (gas-phase) ligands was calculated with the assumption that the chemical bond vibration modes do not change significantly. Entropies were assumed to be negligible in the solid states. The gas-phase ligand entropies were calculated using the Q-Chem 6.1 software package.[13] At room temperature, the total entropies for a gas-phase PEA and DDA (full length) were 0.95 eV and 1.05 eV, respectively.

Supplementary Note 5: Intermolecular interactions

The distance between two closest carbon atoms in different PEAs on a fully passivated $CsPbBr_3$ surface is 4.41 Å. According to reported potential energy curves for benzene dimers, π-π interactions between phenyl rings are attractive when they are spaced by 4.41 Å.[14] The intermolecular interaction between two PEAs was also calculated with wB97x-D/6-311++G** basis set to be – 0.08 eV. This suggests that the intermolecular interaction is attractive.

On the contrary, in the case that the $CsPbBr_3$ surface is fully covered by DDAs (Supplementary Fig. 3), the distance between two closest carbon atoms from different DDAs is less than 4 Å. According to the reported energy curves, the inter-ligand tail interaction would be repulsive.[15] Our calculation showed that the intermolecular interaction between a ligand tail of DDA and all three neighbour carbon chains are repulsive, with an average interaction energy of 0.09 eV. This suggests that DDAs on a fully covered $CsPbBr_3$ surface suffer from steric repulsions, agreeing with previous studies.[11]

Section 3: Additional QD characterizations

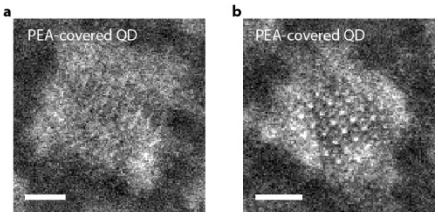

Supplementary Fig. 7 | STEM images of strongly confined PEA-covered $CsPbBr_3$ QDs after solid-state ligand exchange. a, b, PEA-covered QDs maintained their cubical shape after solid-state ligands exchange using PEABr. The scale bars represent a length of 2 nm.

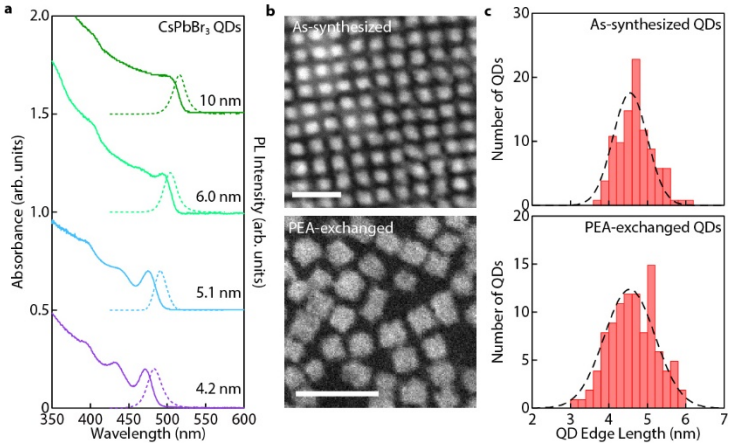

Supplementary Fig. 8 | Absorption spectra and STEM images of $CsPbBr_3$ QDs. a, Absorption (solid curves) and PL (dotted curves) spectra of the $CsPbBr_3$ QDs of various sizes. **b,** HAADF-STEM images of as-synthesized $CsPbBr_3$ QDs (top) and PEA-exchanged QDs (bottom). The scale bars represent a length of 20 nm. Both the as-synthesized QDs and PEA-covered QDs are cubical, suggesting that the solid-state ligand exchange did not change the shape of QDs. **c,** Size histograms of the QDs shown in the TEM images in **b**. The dashed curves are Gaussian fits, resulting in an average size of 4.5 nm. The average size of the QDs remains unchanged after solid-state ligand exchange.

Supplementary Table 1. PLQY of as-synthesized QDs.

QD Size	PL peak wavelength	PLQY
> 10 nm	515 nm	64% ~ 95%
5.1 nm	491 nm	58% ~ 92%
4.2 nm	478 nm	39% ~ 86%
3.6 nm	467 nm	38% ~ 67%
3.0 nm	462 nm	34%

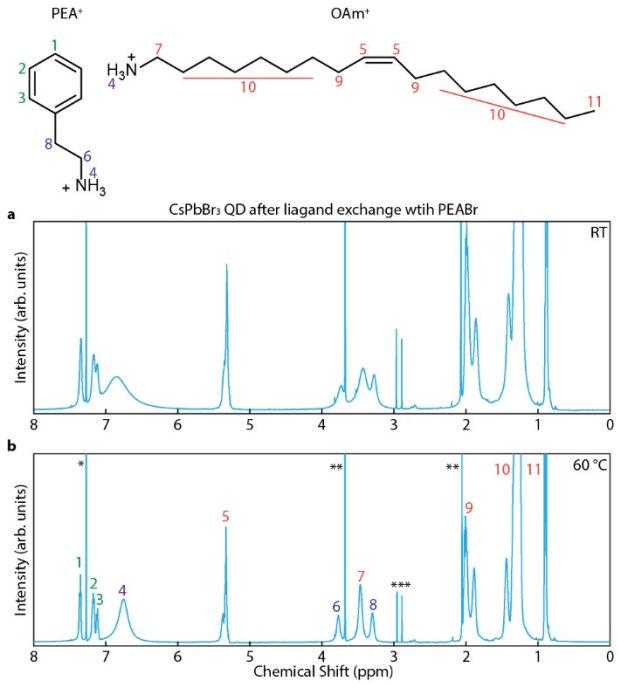

Supplementary Fig. 9 | ^{1}H NMR spectra of $CsPbBr_3$ QDs after solution ligand exchange using PEABr. a, b, ^{1}H NMR spectra of QDs in $CDCl_3$ at **a,** room temperature (RT) and **b,** 60 ˚C.

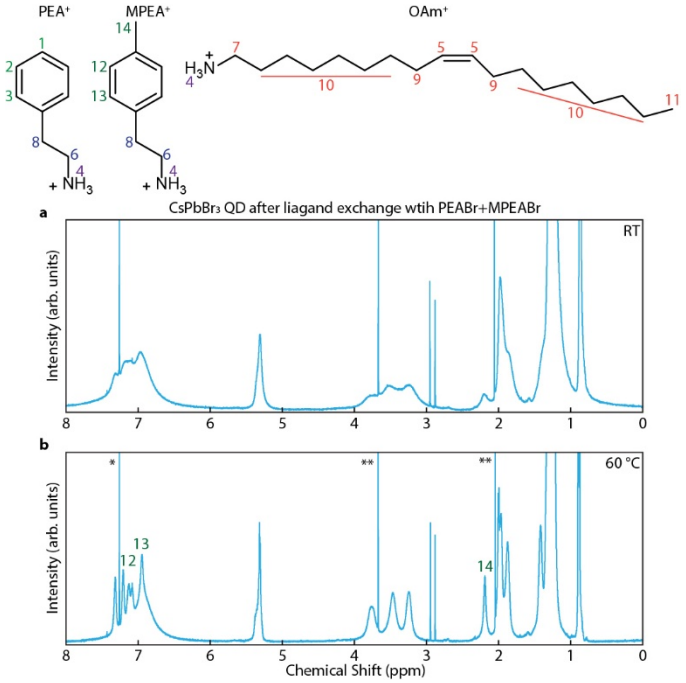

Supplementary Fig. 10 | ^{1}H NMR spectra of $CsPbBr_3$ QDs after solution ligand exchange using a mixture of PEABr and MPEABr. a, b, ^{1}H NMR spectra of QDs in $CDCl_3$ **a,** at room temperature (RT) and **b,** at 60 ˚C.

NMR peak assignments: 1. *p*-phenyl (1H); 2. *m*-phenyl (2H); 3. *o*-phenyl (2H); 6. *α*-methylene (2H); 8. *β*-methylene (2H); 5. olefine (2H); 7. *α*-methylene (2H); 9. allylic methylene (4H); 10. aliphatic methylene (28H); 11. methyl (3H); 12. *m*-phenyl (2H); 13. *o*-phenyl (2H); 14. methyl (3H); the chemical shifts of *α*- and *β*-methylene protons are similar to that of PEABr; and 4. ammonium. All the sharp peaks labelled with *(chloroform), **(methyl acetate) and ***(*N,N*-dimethylformamide) are solvent residues introduced during the ligand exchange.

The broadening of the ^{1}H NMR peaks at room temperature suggests that the PEA^{+} moieties are bound to the QD surface. To better resolve the phenyl protons in PEA and MPEA, the samples were heated to 60 °C. The QD samples showed no signs of degradation after heating.

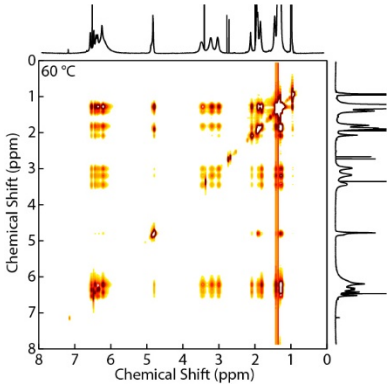

Supplementary Fig. 11 | 2D NOESY of $CsPbBr_3$ QDs after solution ligand exchange using a mixture of PEABr and MPEABr. The spectrum was collected at 60 °C.

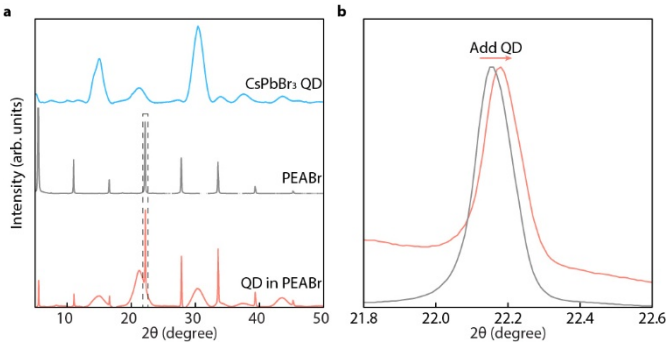

Supplementary Fig. 12 | XRD pattern of solid-state ligand exchanged $CsPbBr_3$ QDs. a, XRD patterns of pristine $CsPbBr_3$ QDs (green), pristine PEABr thin-film (blue) and PEABr thin-film with high concentrations of solid-state ligand exchanged QDs (red). **b,** When QDs are added, the PEABr peaks exhibit a small shift towards a higher angle, indicating potential intermolecular spacing change induced by forming epitaxial interfaces with $CsPbBr_3$ QDs**.**

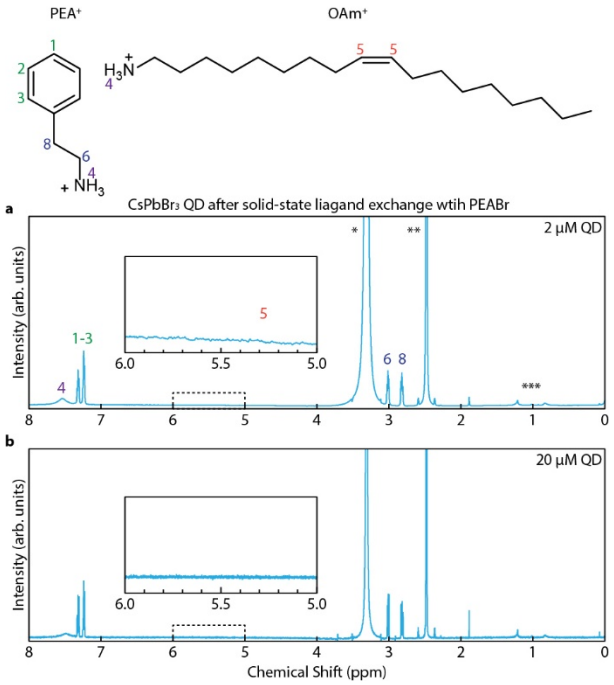

Supplementary Fig. 13 | ^{1}H NMR spectra of digested $CsPbBr_3$ QDs after solid-state ligand exchange using PEABr. a, b, The solid-state ligand exchanges were using **a,** 2 μM and **b,** 20 μM of QD colloids, which are ~ 10^4× and ~ 10^5× more concentrated than that used for single QD sample preparations, respectively. The sample film was digested using deuterated dimethyl sulfoxide (DMSO-d_6) for ^{1}H NMR measurements. The insets show zoom-in views of the NMR spectra between 5 and 6 ppm, where the olefin proton signals of oleylammonium is expected. No olefin proton signal is observed even with the significantly higher QD concentration used in this experiment. Peaks labelled with * (water), ** (DMSO) and *** (octane) are solvent residues.

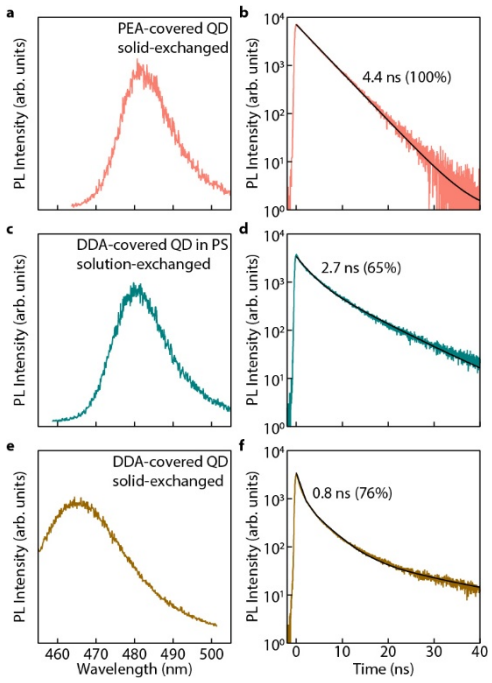

Supplementary Fig. 14 | Single QD samples prepared using DDABr during the solid-state ligand exchange. a, c, e, PL spectra and **b, d, f,** Time-dependent PL intensity decay traces of single $CsPbBr_3$ QDs from the same batch (~ 4.3 nm), prepared by **a, b,** solid-state ligand exchange using PEABr (sample of interest), **c, d,** solution ligand exchange with DDABr (using reported method[16]) and **e, f,** solid-state ligand exchange with DDABr (using our method). The Time-dependent PL intensity decay traces are fitted with mono- or bi-exponential functions. The time constants of the initial fast decay component are shown in the figure. Faster decay often suggests intensive exciton trapping. The QD that underwent DDA solid exchange showed severe exciton trapping. Additionally, the PL blueshift of this QD indicates ligand exchange-induced degradation.

Section 4: Single QD PL data analyses

Supplementary Note 6: Mandel Q parameter

The distribution of the PL ON state is characterized using normalized second factorial moment minus one (Mandel Q parameter):

$$Q = \frac{\langle \Delta C^2 \rangle - \langle C \rangle}{\langle C \rangle} = \frac{\sigma^2}{\mu} - 1 \quad (1)$$

where C is the photon counts per bin in the blinking trace, ΔC is the deviation of photon counts from the expected value, and the bracket denotes the mean value over the measurement time. The Q parameter can also be expressed as the square of the standard deviation, σ, of the photon counts, divided by the mean value μ, then minus 1. The Q value is zero for a Poisson distribution, the characteristic of a shot-noise limited PL ON state distribution. The Q typically rises above 1 if the PL ON state intensity is fluctuating (i.e. multiple emissive states are mixed).[17] To examine the ON state Q parameter, we fit the intensity distribution histogram with a Gaussian curve, taking the mean value and standard deviation for Q parameter calculations.

Supplementary Note 7: Average excitation number

For single QDs excited using a pulsed mode laser, the average excitation number per pulse, $\langle N \rangle$, is calculated using the following equation:

$$\langle N \rangle = \frac{fP}{R\pi r^2} \frac{\lambda}{hc} \sigma \quad (2)$$

where P is the average laser power, R is the pulse repetition rate (typically 2 – 5 MHz), and r is the Gaussian beam spot radius (~ 475 nm), f is a beam position factor with the value of 2 (assuming QD is at the centre of the Gaussian laser beam spot), λ is the laser wavelength (405 nm), h is Planck's constant, c is the speed of light, and σ is the optical cross-section of the QD using literature values.[18] The calculated $\langle N \rangle$ value is subject to the uncertainty in the laser beam spot radius and the positioning of the emitter with respect to the beam. In this work, the $\langle N \rangle$ value is cross-examined using the detected photon count rates.

Supplementary Note 8: Saturation single QD emission count rate

The overall saturation count rate of a single QD emission (I_{sat}) under the *cw* excitation is limited by the exciton radiative rate of the QD (k_r) with the first-order approximation that $I_{sat} \approx k_r$. As a result, I_{sat} is estimated to be ~ 200 MHz for strongly confined $CsPbBr_3$, ~ 100 MHz for weakly confined $CsPbBr_3$, and ~ 70 MHz for $CsPbI_3$.

The overall photon detection efficiency (η) determines the measurable count rate at saturation excitation. For our instrument, η is ~ 0.09 at 470 nm (strongly-confined $CsPbBr_3$ QDs), ~ 0.08 at 515 nm (weakly-confined $CsPbBr_3$ QDs), and ~ 0.03 at 650 nm ($CsPbI_3$ QDs). The overall QD emission count rate can then be calculated as the measured average ON state count rate divided by η of the corresponding wavelength.

Section 5: Additional single QD spectroscopic measurements

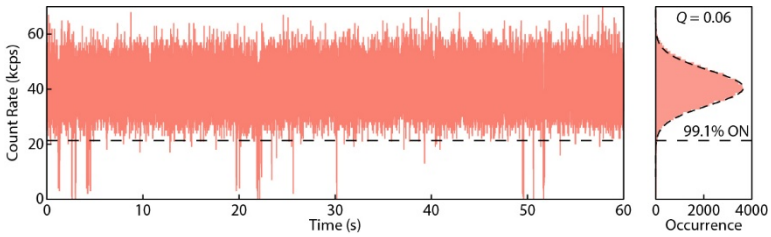

Supplementary Fig. 15 | PL blinking trace and intensity distribution histogram of the PEA-covered QD shown in Fig. 2 with a 1 ms bin time. The ON fraction time remains high (> 99%), and the PL intensity distribution remains shot-noise limited ($Q \approx 0$).

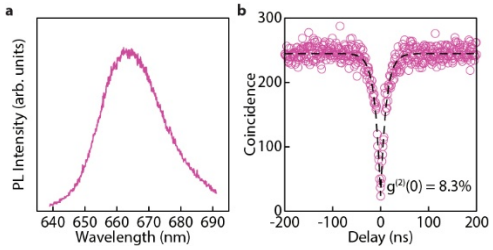

Supplementary Fig. 16 | Optical properties of the single 7.0 nm PEA-covered $CsPbI_3$ QD shown in Fig. 2. a, PL spectrum. **b,** Second-order correlation plot, with a $g^{(2)}(0)$ value of 8.3% after background correction.

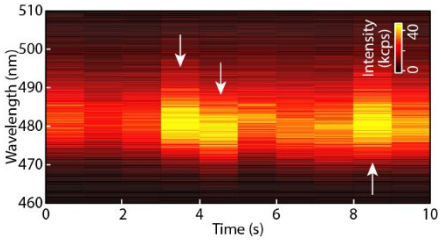

Supplementary Fig. 17 | PL spectra diffusion in a DDA-covered $CsPbBr_3$ QD. The integration time of PL spectrum collection is 1 s. The arrows indicate when spectral diffusion happens.

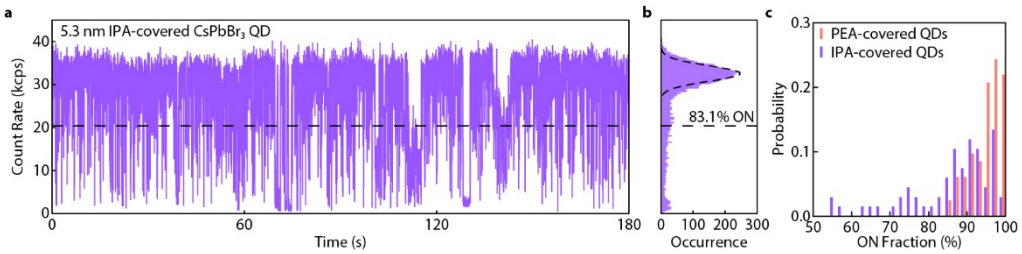

Supplementary Fig. 18 | Blinking behaviour of IPA-covered $CsPbBr_3$ QDs. a, A typical PL blinking trace (10 ms bin time) of a 5.3 nm IPA-covered $CsPbBr_3$ QD. **b,** The corresponding PL intensity distribution histogram. **c,** Histograms of ON time fraction of 67 IPA-covered QDs (purple), and 81 PEA-covered QDs (red). Despite exhibiting suppressed blinking, the average ON time fraction of IPA-covered QD (83%) is lower than that of PEA-covered QDs (95%). Additionally, the IPA-covered QDs show a larger ON time fraction variance.

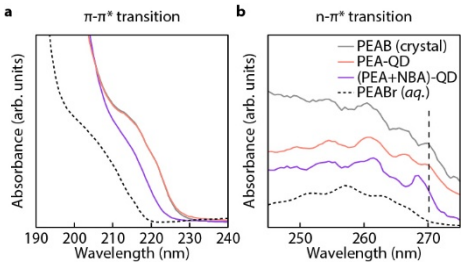

Supplementary Fig. 19 | Thin-film linear absorption spectra. a, Absorption spectra in the π – π* transitions spectral region of a pristine PEABr polycrystalline thin film (grey), QD in PEABr after the solid-state ligand exchange (orange), QD in a mixture of 3:1 ratio of PEABr and NBABr after solid-state ligand exchange (purple), and PEABr aqueous solution (black dotted curves). **b,** Absorption spectra in the n – π* transitions spectral region.

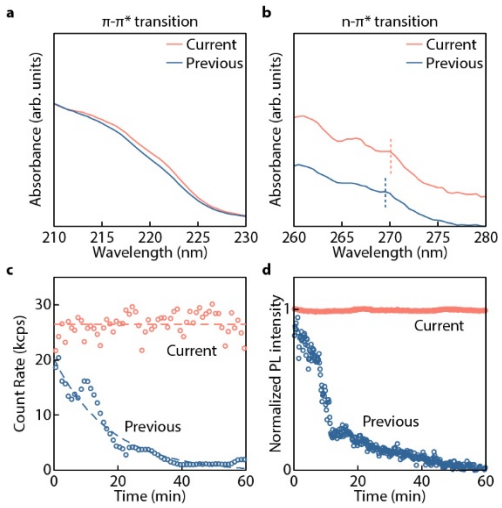

Supplementary Fig. 20 | Photostability of $CsPbBr_3$ QDs in PEABr without ligand tail engineering. a, b, Absorption spectra of QDs in PEABr sample using solution-engineering ligand exchange in this work (orange) and in our previous work[19] (blue) in **a,** the $\pi - \pi^*$ transitions spectral region and **b,** the $n - \pi^*$ transitions spectral region (offset for display clarity). **c,** PL intensities of a single $CsPbBr_3$ QD prepared using the previous method[19] (blue), measured over 1 h of continuous laser excitation, binned every 10 ms, and averaged over every 1 min (dashed curves are visual guides). **d,** Normalized PL intensity of a collection of QDs prepared using the previous method (blue) under 1 h of continuous laser excitation. The PL intensity traces of QDs prepared using the current method (orange) are plotted for comparisons: **c,** a single QD (extracted from Supplementary Fig. 22a below, measurements in the 4th hour are shown since the interference of sample stage drifting was insignificant); **d,** a collection of single QDs (extracted from Fig. 4f).

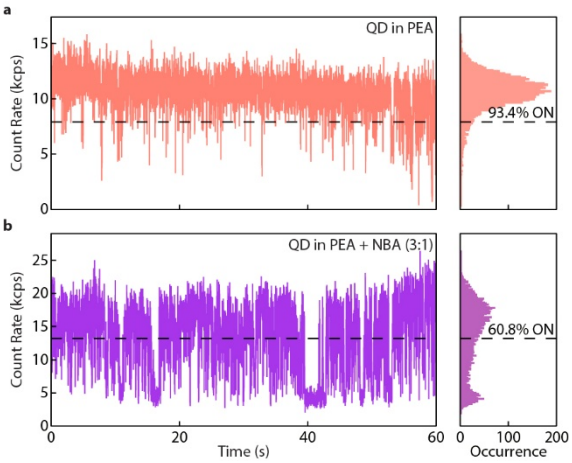

Supplementary Fig. 21 | Additional PL blinking traces and intensity distribution histograms of samples used for low-frequency Raman measurements. a, A PEA-covered $CsPbBr_3$ QD in PEABr matrix. **b,** A $CsPbBr_3$ QD solid-state ligand exchanged with a mixture of PEABr and NBABr. All blinking traces are built with a bin time of 10 ms.

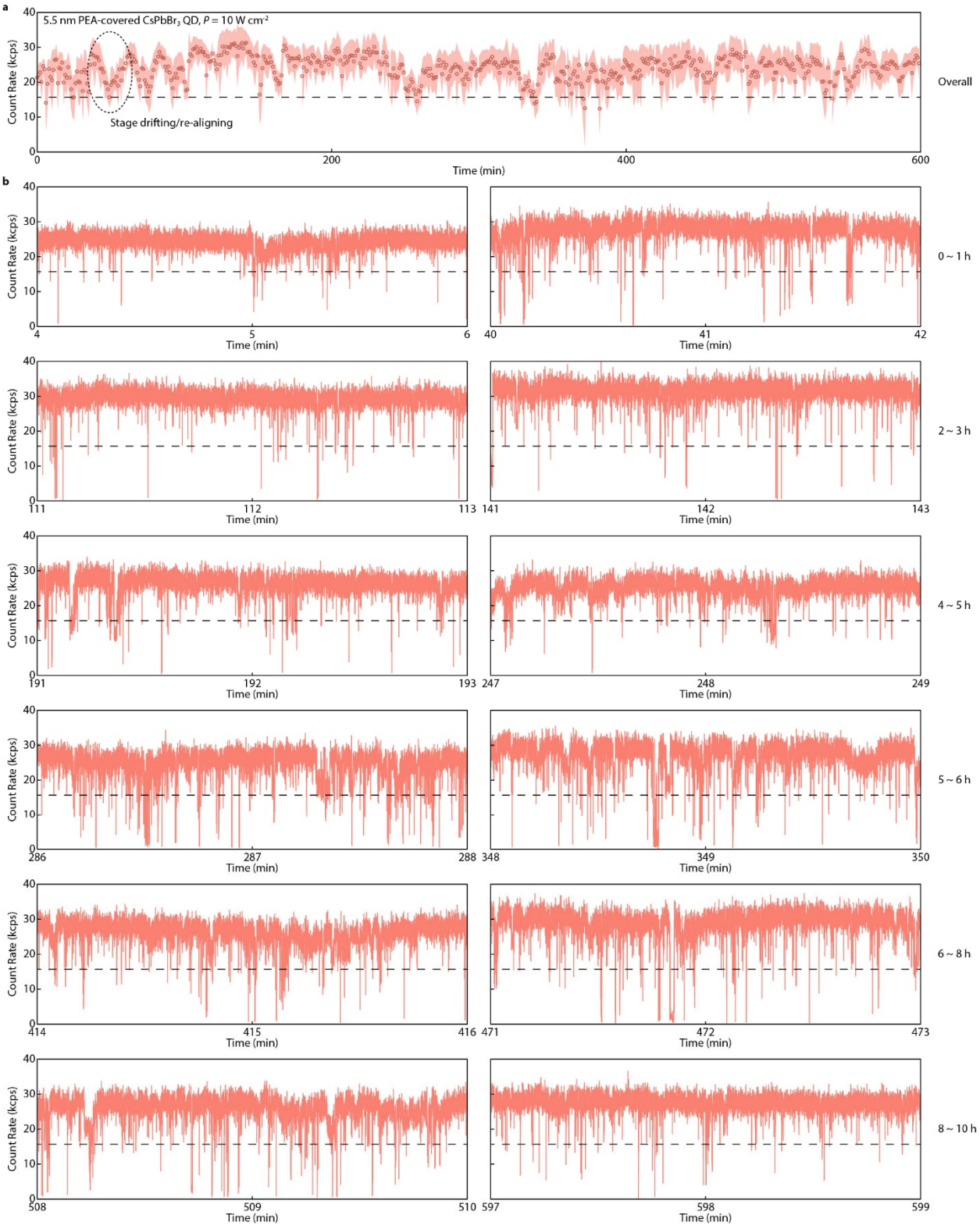

Supplementary Fig. 22 | The 10-h continuous blinking measurement of a single $CsPbBr_3$ QD. a, The overall PL intensity trace is binned every 10 ms and averaged every 1 min. The shaded area marks the standard deviation. Intensity fluctuations (indicated in the dashed circle) are largely due

to random sample stage drifting and the necessary re-alignments every few minutes. The QD was excited with 405 nm laser at an intensity of 10 W cm^{-2}. **b,** 2-min segments of the blinking trace.

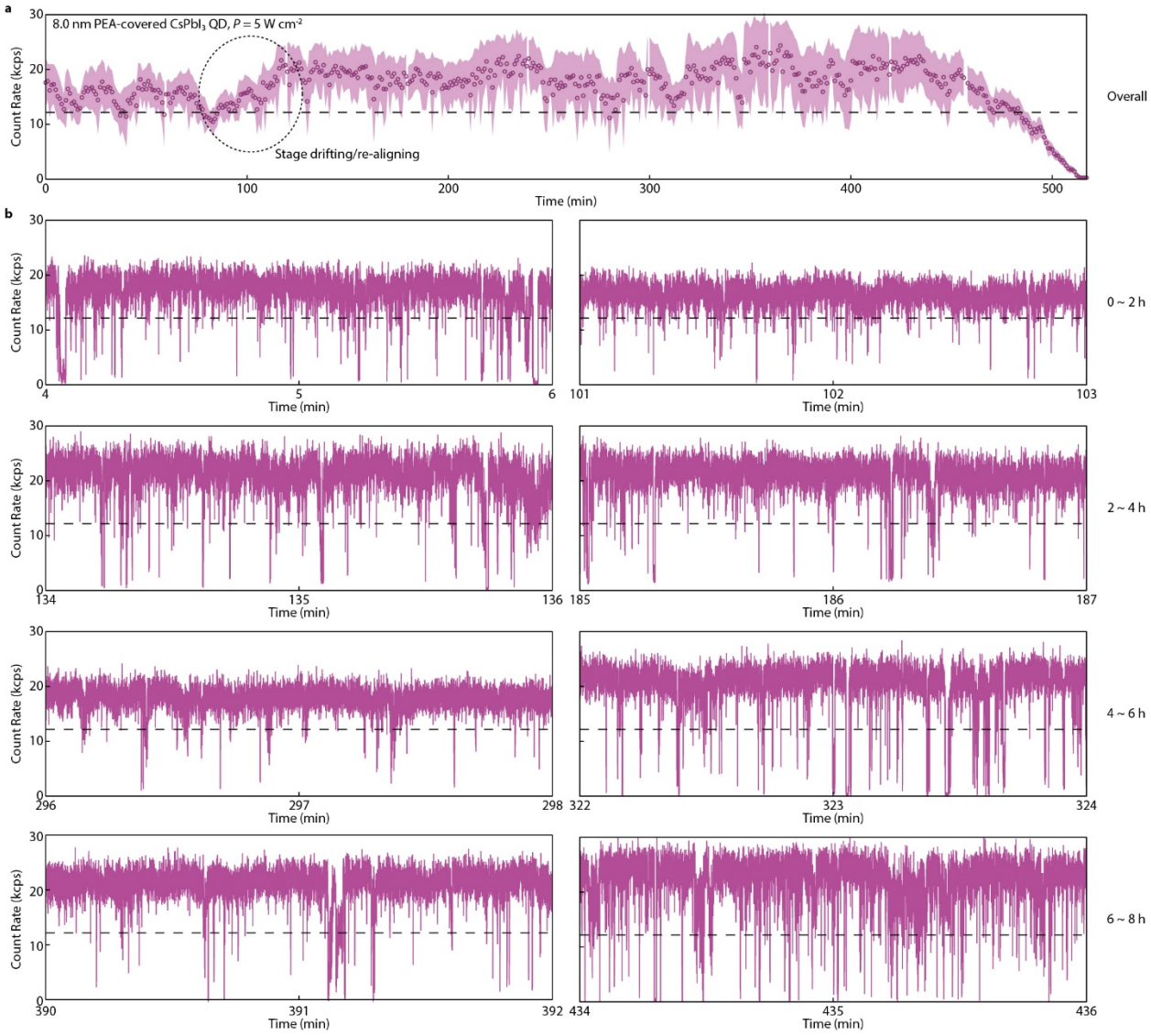

Supplementary Fig. 23 | The 8.5-h continuous blinking measurement of a single $CsPbI_3$ QD. **a,** The overall PL intensity trace is binned every 10 ms and averaged every 1 min. The shaded area marks the standard deviation. Intensity fluctuations (indicated in the dashed circle) are largely due to random sample stage drifting and the necessary re-alignments every few minutes. The QD was excited with 405 nm laser at an intensity of 5 W cm^{-2}. **b,** 2-min segments of the blinking trace.

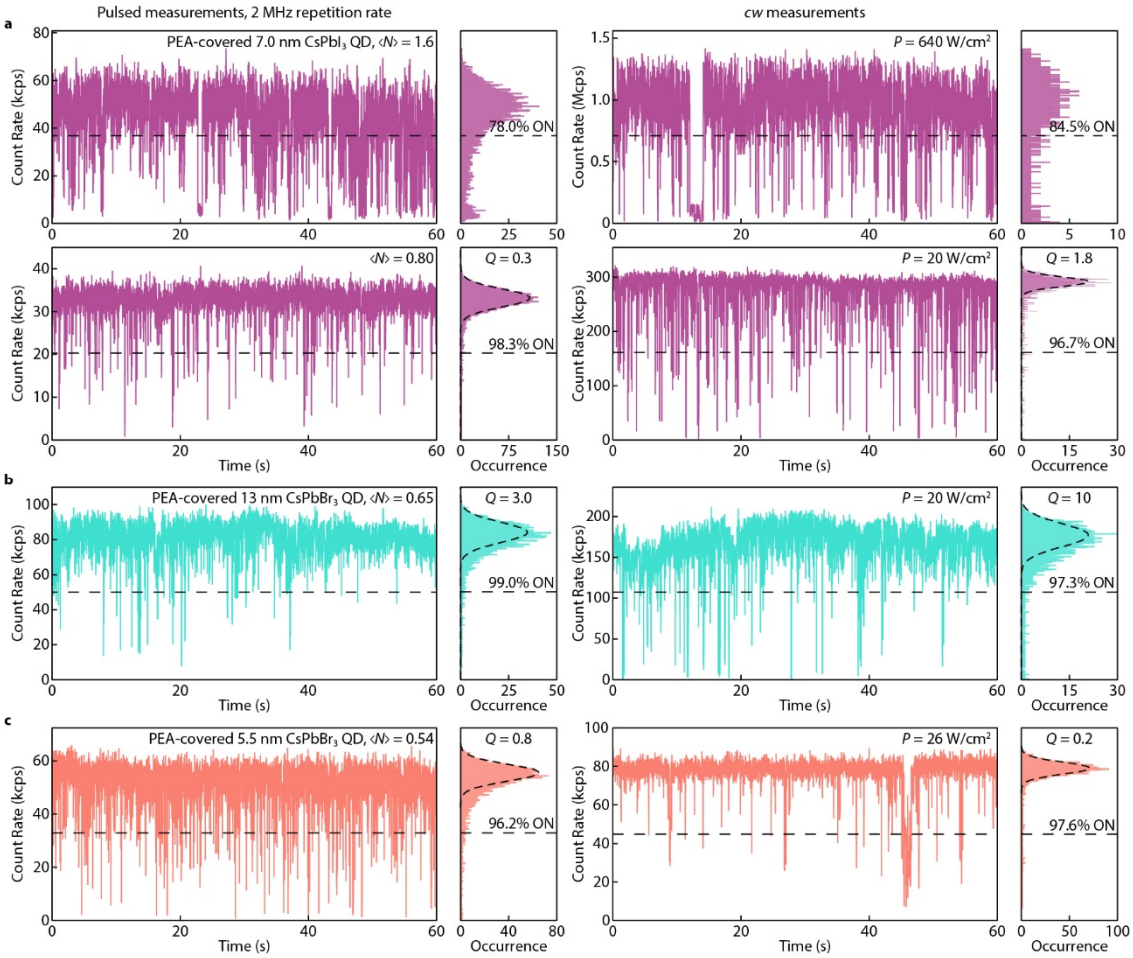

Supplementary Fig. 24 | Blinking traces of single PEA-covered QDs under intense excitations. **a – c,** Blinking traces and PL intensity distribution histograms of **a,** a 7.0 nm $CsPbI_3$ QD, **b,** a 13 nm $CsPbBr_3$ QD and **c,** a 5.5 nm $CsPbBr_3$ QD, using both pulsed (2 MHz, left column) and *cw* excitation conditions. All blinking traces are built with a bin time of 10 ms. The excitation densities/power densities were noted in the figures. When the excitation density approaches saturation, the *Q* parameter of the blinking traces increases.

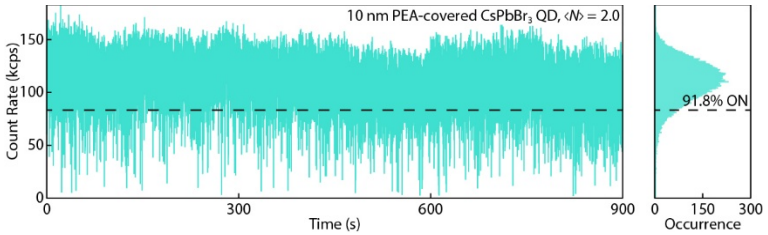

Supplementary Fig. 25 | PL blinking trace and intensity distribution histogram of a single 10 nm PEA-covered $CsPbBr_3$ QD under an excitation rate beyond saturation. The blinking trace is built with a bin time of 10 ms. The QD exhibits 91.8% ON time over 15 min of measurement without photodarkening.

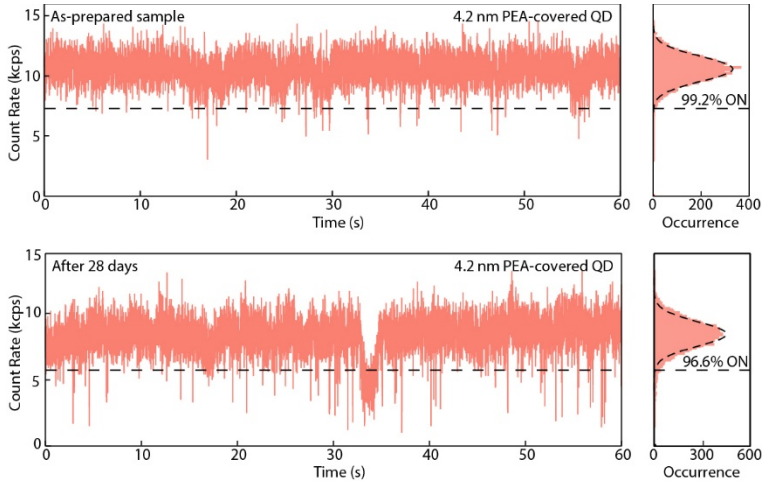

Supplementary Fig. 26 | Blinking traces of a PEA-covered QD sample after ~ 1 month storage at ambient conditions. The blinking traces are built with a bin time of 10 ms. The PEA-covered QD remained nearly non-blinking with a > 96% ON time fraction.

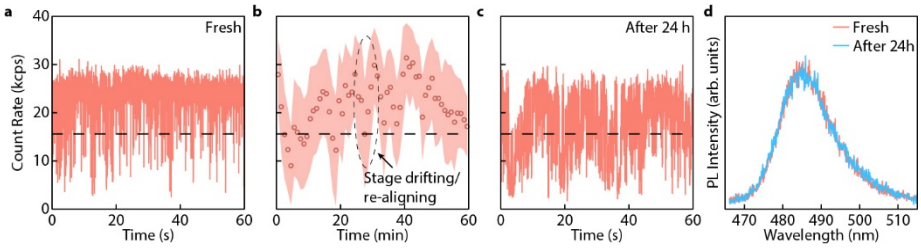

Supplementary Fig. 27 | PL performance of a PEA-covered QD sample without encapsulation. a, PL blinking trace of a 4.5 nm PEA-covered $CsPbBr_3$ QD on a freshly prepared sample film. **b,** PL intensity trace of the same QD over 1 h, binned every 10 ms and averaged every 1 min. The shaded area marks the standard deviation. Intensity fluctuations (indicated in the dashed circle) are largely due to random sample stage drifting and the necessary re-alignments every few minutes. **c,** PL blinking trace of the same QD, exposed to ambient environment (21 °C, 30% ~ 50% relative humidity) for 24 h. All blinking traces were built using a bin time of 10 ms. **d,** PL spectra of the QD before and after the 24 h exposure.

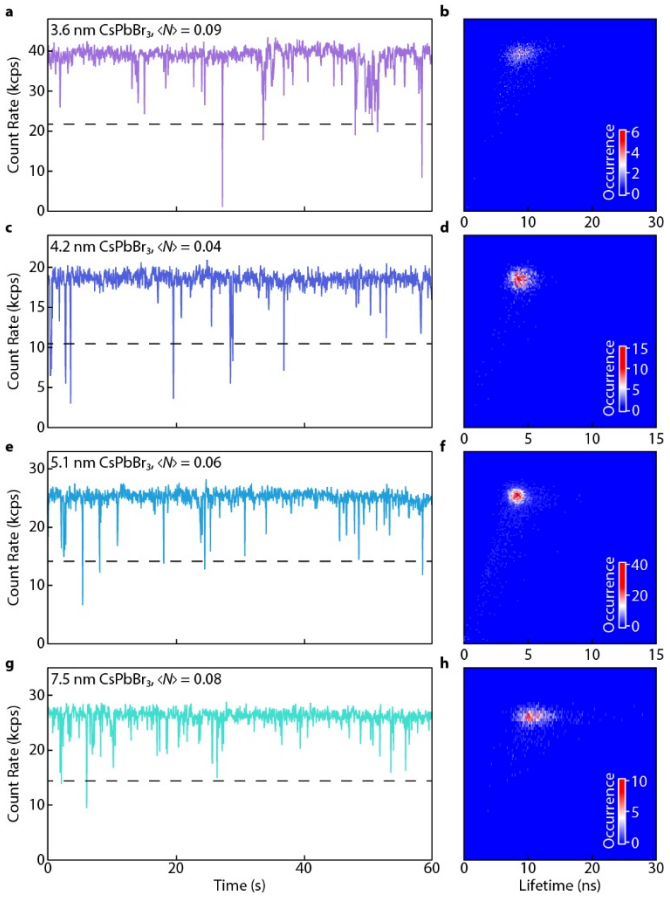

Supplementary Fig. 28 | Fluorescence lifetime-intensity distribution (FLID) analyses. a, c, e, g, Replotted blinking traces shown in Fig. 5a – 5d using a bin time of 50 ms (to improve the signal-to-noise ratio for the FLID analyses). **b, d, f, h,** Corresponding FLID heatmaps.

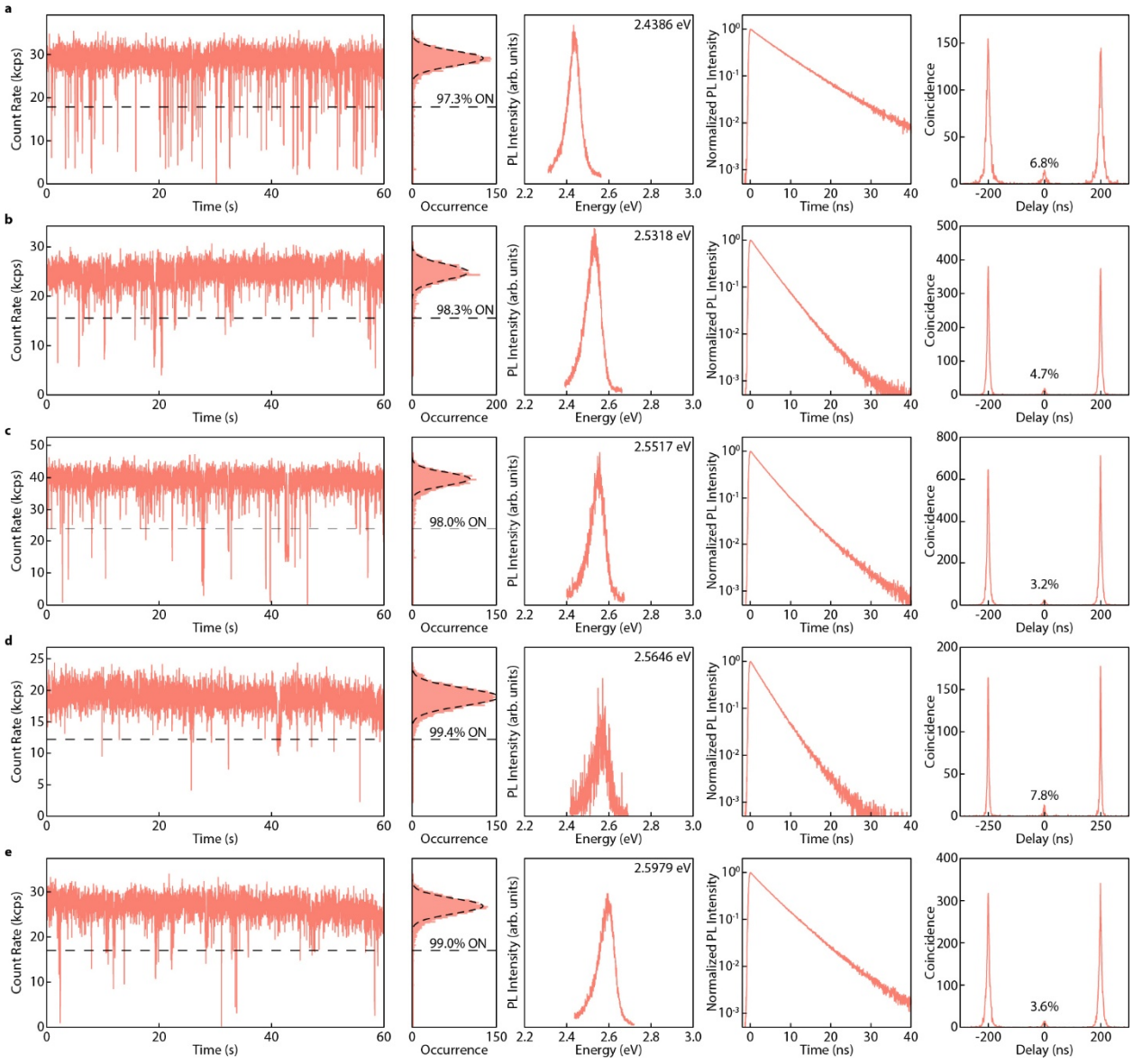

Supplementary Fig. 29 | Additional single QD spectroscopic measurements. a – e, PL blinking traces (first column, with a bin time of 10 ms), intensity distribution histograms (second column), spectra (third column), time-resolved PL decay traces (fourth column), and second-order correlation plots (fifth column) of five different PEA-covered $CsPbBr_3$ QDs.

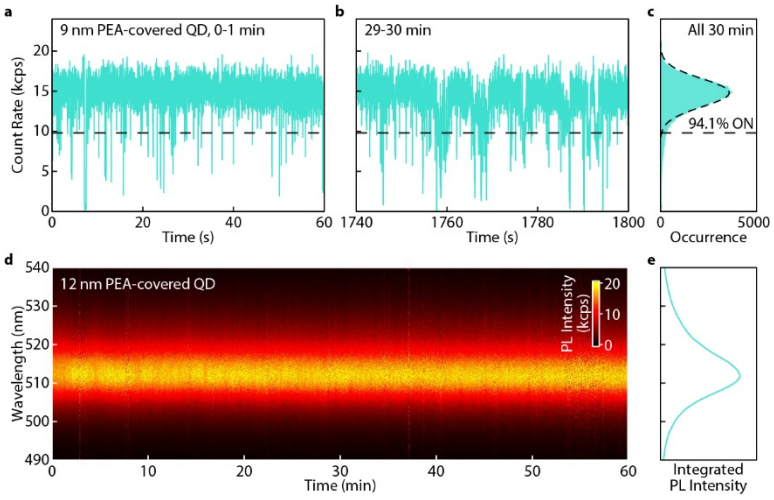

Supplementary Fig 30 | Suppressed blinking and spectral diffusion of single weakly confined PEA-covered $CsPbBr_3$ QD. a, b, PL blinking traces (with a bin time of 10 ms) of a weakly confined PEA-covered $CsPbBr_3$ QD (9 nm) in a 1-miunte window at **a** the first and **b** the last minute of a 30-minute continuous measurement. **c,** PL intensity distribution histogram built using the entire 30-minute measurements. **d,** Normalized time-dependent PL spectra of a weakly confined PEA-covered $CsPbBr_3$ QD (12 nm) measured continuously for 1 h. No spectral diffusion or shifting are observed. **e,** Integrated PL spectrum from **d**. Its FWHM remains small (69 ± 1 meV) and comparable to that (69 ± 2 meV) of the PL spectrum measured in a short time window (60 s), suggesting the PL of the QD was stable.

Section 6: Statistical considerations of the photophysical properties of the single QDs

Supplementary Note 9: Second-order correlation and single photon purity

The second-order correlation ($g^{(2)}$) analyses on the PL emission of single QDs yield a $g^{(2)}(0)$ value, and 1 - $g^{(2)}(0)$ value is typically considered the single photon purity. This $g^{(2)}(0)$ value in non-blinking and binary blinking QDs represents the ratio of the quantum yield of biexcitons to that of excitons, the latter of which is typically considered unity.[20] Given the fast biexciton Auger recombination rates in strongly confined $CsPbBr_3$ QDs (~ 20 ps), the theoretical $g^{(2)}(0)$ value of strongly confined QDs can reach ~ 0.02, which is close to our average $g^{(2)}(0)$ values (0.054). According to reported discussions, the $g^{(2)}(0)$ values will increase when there are intermediate emissive states, such as grey states and emissive trion states.[21] Almost all defects are passivated in our nearly non-blinking QDs, and the intermediate emissive states are largely removed (manifested as low Q parameters). Therefore, our study's smaller $g^{(2)}(0)$ values (Supplementary Fig. 30) are attributed to the suppressed blinking.

Supplementary Note 10: Size-dependent exciton radiative rates

The rate of spontaneous emission transition rate between the excitonic state (ex) and the ground state can be derived from Fermi's golden rule:

$$\Gamma_{ex} \propto \omega_{ex} |\langle 0|\boldsymbol{p}|ex\rangle|^2 \quad (3)$$

where Γ_{ex} is the transition rate, $|\langle 0|\boldsymbol{p}|ex\rangle|$ is the matrix element, and ω_{ex} is the frequency of light emitted by the exciton. Therefore, the transition rate is proportional to the emission frequency, which increases with decreasing size in the case of QDs.

When considering the exciton fine structure, the exciton can be modelled as a three-state system, where the exciton state is further split into an optically active bright triplet state and an optically passive dark singlet state.[22] Radiative recombination of the dark exciton is partially forbidden and slow (~μs scale[23]). When perovskite QDs are experiencing strong quantum confinement, the dark state becomes the ground state.[22] Then, the apparent radiative recombination rate is determined by the relative thermal occupation of the bright and dark excitonic states. The energy spacing between bright and dark states increases with decreasing QD size. When the splitting becomes significant (i.e. > 10 meV for < 4.5 nm QDs) compared to kT, increasing contribution from the dark state will slow down the apparent radiative recombination rate. Similar size-dependent radiative rates were also observed in conventional II-VI QDs.[24] In addition, we have observed similar phenomena using ensemble $CsPbBr_3$ QDs with narrow size distributions (Supplementary Fig. 31). The radiative rates obtained in our study agree well with recently reported values.[25]

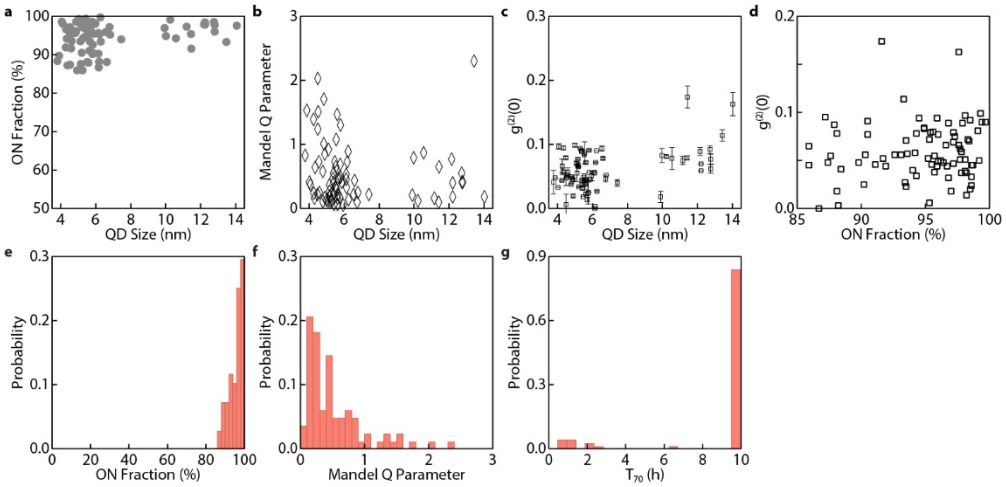

Supplementary Fig. 31 | Statistics of PL properties of $CsPbBr_3$ QDs. a, PL ON fractions, **b,** Mandel *Q* parameters, and **c,** $g^{(2)}(0)$ values of 81 single QD measurements with respect to the QD sizes. The error bars shown on $g^{(2)}(0)$ values indicate the standard deviation. 60 of the 81 QDs are strongly confined (size < 7.0 nm), with an average $g^{(2)}(0)$ value of 0.054. **d,** $g^{(2)}(0)$ values plotted against the PL ON fraction of each QD. No significant correlation was observed. **e, f,** Probability histograms of **e,** PL ON fraction and **f,** Mandel *Q* parameter of these QDs. These statistics are built from 81 single PEA-covered $CsPbBr_3$ QD PL measurements. **g,** Probability histogram of the duration distribution for QD survival times (defined as the time it takes to reach 70% of the initial PL intensity, T_{70}, when QDs show photodarkening). Most QDs did not show intensity decay over 10 h since the sample stage drifting limits the measurement time. This histogram is built by meshing the PL image obtained from the 10 h measurement described in Fig. 4f.

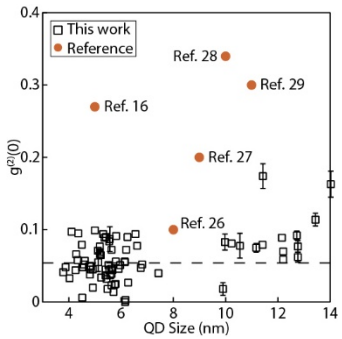

Supplementary Fig. 32 | Reported $g^{(2)}(0)$ values of single $CsPbBr_3$ QDs.[16, 26–29] Each open square represents a group of QDs with similar size measured in this work. The dashed line is a visual guide that marks the average $g^{(2)}(0)$ value of 0.054 for our strongly confined QDs (< 7 nm).

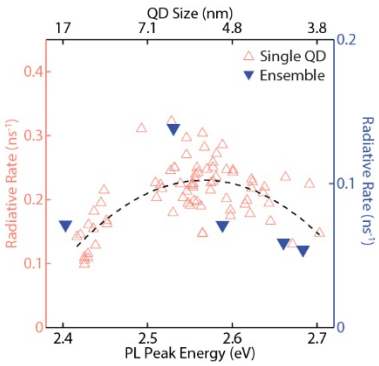

Supplementary Fig. 33 | Radiative rates of QD colloids compared to that of single QDs. Statistics of exciton radiative recombination rates of 81 non-blinking PEA-covered $CsPbBr_3$ QDs (red open triangles) and five as-synthesized QD colloids (blue solid triangles) with different sizes. The dashed curve is a visual guide. The radiative rates of colloidal QDs are corrected by their quantum yield.[30] The overall lower radiative rate can be attributed to the smaller dielectric constant of hexane compared to PEABr solids.[31, 32]

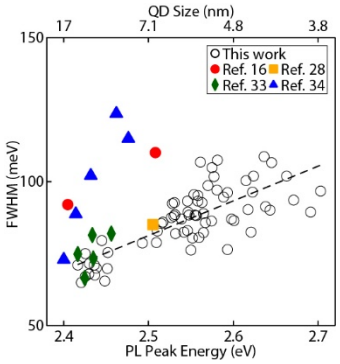

Supplementary Fig. 34 | Reported single $CsPbBr_3$ QD PL linewidths.[16, 28, 33, 34] The full-width half-maximum (FWHM) values are plotted for comparison. The dashed line is a linear fit of the linewidths measured in this work.

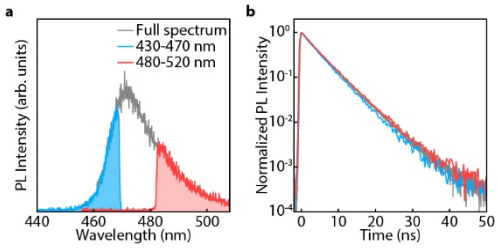

Supplementary Fig. 35 | Spectral independent PL decay dynamics. a, PL spectrum of a PEA-covered single $CsPbBr_3$ QD. **b,** Time-resolved PL intensity decay measured at different spectral windows (color-coded) selected using bandpass filters.

Supplementary Table 2. Emission performance of single $CsPbBr_3$ perovskite QDs

QD size	Reported excitation density	ON state count rate (rep. rate)	PL ON fraction	Mandel *Q* parameter	Photostability (estimated)	Single photon purity	Reference
8-10 nm	0.15 ~ 0.24	185 kcps (10 MHz)	80%	< 1	150 s	89%	Sup. Ref [35]
10 nm	-	-	-	-	-	73% (avg.)	Sup. Ref [28]
12 nm	0.09	30 kcps (5 MHz)	80%	24	300 s	-	Sup. Ref [36]
10 nm	0.2	25 kcps (10 MHz)	-	-	300 s	74%	Sup. Ref [29]
12 nm	3	60 kcps (2.5 MHz)	> 90%	3	600 s	0-92%	Sup. Ref [37]
5 nm	0.2	60 kcps (10 MHz)	78%	8	40 s	78%	Sup. Ref [16]
3.6 nm (thickness) 11.3 nm (lateral)	-	7.5 kcps (2.5 MHz)	68%	-	20 min	80% (median)	Sup. Ref [38]
3.6-14 nm	0.80 (strongly-confined)	89 kcps (2 MHz)	95% (avg.)	0.57 (avg.)	12 h	95% (avg.)	This work
		300 kcps (*cw*)					
	1.1 (weakly-confined)	160 kcps (2 MHz)					
		1300 kcps (*cw*)					

Supplementary Table 3. Emission performance of single $CsPbI_3$ perovskite QDs

QD size	Reported excitation density	ON state count rate (rep. rate)	PL ON fraction	Mandel *Q* parameter	Photostability (estimated)	Single photon purity	Reference
9.8 nm	3.3	60 kcps (2.5 MHz)	86%	47	600 s	94% (avg.)	Sup. Ref [39]
9.3 nm	1.7	75 kcps (5 MHz)	> 80%	< 1	300 s	95%	Sup. Ref [40]
6.6 nm	~ 0.7	65 kcps (10 MHz)	92%	10	100 s	90% (avg.)	Sup. Ref [28]
5.0-8.0 nm	~ 1.6	60 kcps (2 MHz) 1100 kcps (*cw*)	92% (avg.)	0.16 (avg.)	7 h	98% (avg.)	This work

Section 7: Methods and instrumentation

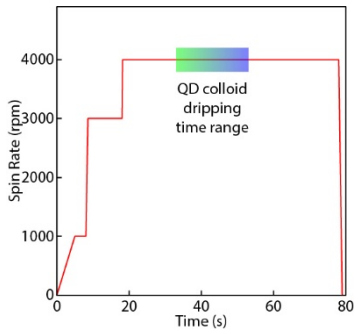

Supplementary Fig. 36 | Spin coating program and parameters. The red curve shows the programmed spin rate and stepped acceleration. The gradient colour window indicates the optimized time range for dripping the QD colloids to achieve solution-engineering ligand exchange. The exact dripping time depends on the QD size (earlier dripping time for larger QD).

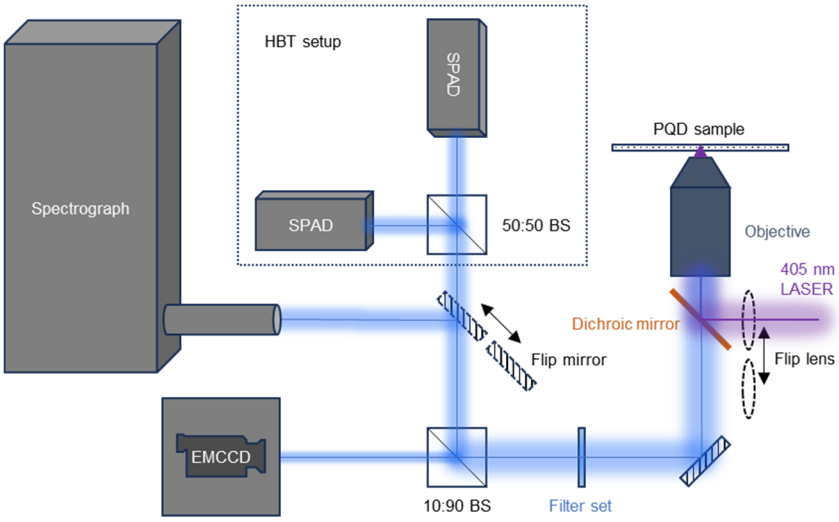

Supplementary Fig. 37 | Schematic illustrations of the single particle microscope setup. Stages, mirrors and focusing lenses are omitted. The filter set consists of a 405 nm notch filter, a 425 nm long pass filter, and a selected bandpass filter when needed.

The 405 nm laser (pulsed/*cw*) was attenuated with a set of reflective/absorptive neutral density filters, and then sent to a single-mode optical fibre. Only the TEM00 mode was allowed to pass through the fibre and then collimated. The average laser power is typically measured after this point and calibrated using a microscope slide power meter sensor head (Thorlabs, S171C) measuring after the objective. In confocal mode, the collimated TEM00 mode laser was sent through the objective and focused to a Gaussian spot on the sample plane. The spot diameter (where the irradiance > $1/e^2$ of the maximum) is measured to be ~ 475 nm using a fluorescence standard. Due to the QD size (a few nm) being significantly smaller than the beam size, the QD is considered a dimensionless point when calculating the power density of the focused beam. At the peak of the Gaussian beam profile, the power density is twice of the average power density of the

entire beam spot area. When imaging QDs in wide-field mode, the flip lens is set to intercept the beam path, de-collimating the laser beam and focusing it near the back focal plane of the objective.

Supplementary References

1. Kresse, G.; Furthmüller, J. Efficiency of ab-initio total energy calculations for metals and semiconductors using a plane-wave basis set, *Comput. Mater. Sci.* **6,** 15-50 (1996).

2. Kresse, G.; Furthmüller, J. Efficient iterative schemes for ab initio total-energy calculations using a plane-wave basis set, *Phys. Rev. B* **54,** 11169-11186 (1996).

3. Perdew, J. P.; Burke, K.; Ernzerhof, M. Generalized Gradient Approximation Made Simple, *Phys. Rev. Lett.* **77,** 3865-3868 (1996).

4. Grimme, S.; Antony, J.; Ehrlich, S.; Krieg, H. A consistent and accurate ab initio parametrization of density functional dispersion correction (DFT-D) for the 94 elements H-Pu, *J. Chem. Phys.* **132,** (2010).

5. Grimme, S.; Ehrlich, S.; Goerigk, L. Effect of the damping function in dispersion corrected density functional theory, *J. Comput. Chem.* **32,** 1456-1465 (2011).

6. Grazulis, S. *et al.* Crystallography Open Database - an open-access collection of crystal structures, *J. Appl. Crystallogr.* **42,** 726-729 (2009).

7. Stoumpos, C. C. *et al.* Crystal Growth of the Perovskite Semiconductor $CsPbBr_3$: A New Material for High-Energy Radiation Detection, *Cryst. Growth Des.* **13,** 2722-2727 (2013).

8. Hjorth Larsen, A. *et al.* The atomic simulation environment—a Python library for working with atoms, *J. Condens. Matter Phys.* **29,** 273002 (2017).

9. Pulay, P. Convergence acceleration of iterative sequences. the case of scf iteration, *Chem. Phys. Lett.* **73,** 393-398 (1980).

10. Rademeyer, M. 2-Phenylethylammonium bromide, *Acta Cryst.* **E63**, o221-o223 (2007).

11. Imran, M. *et al.* Simultaneous cationic and anionic ligand exchange for colloidally stable $CsPbBr_3$ nanocrystals. *ACS Energy Lett.* **4**, 819–824 (2019).

12. Quarta, D. *et al.* Stable ligand coordination at the surface of colloidal $CsPbBr_3$ nanocrystals. *J. Phys. Chem. Lett.* **10**, 3715–3726 (2019).

13. Epifanovsky, E. *et al.* Software for the frontiers of quantum chemistry: an overview of developments in the Q-Chem 5 package. *J. Chem. Phys.* **155**, 084801 (2021).

14. Sherrill, C. D.; Takatani, T.; Hohenstein, E. G. An assessment of theoretical methods for nonbonded interactions: comparison to complete basis set limit coupled-cluster potential energy curves for the benzene dimer, the methane dimer, benzene−methane, and benzene−H_2S. *J. Phys. Chem. A* **113**, 10146–10159 (2009).

15. Bursch, M.; Grimme, S.; Hansen, A. Influence of steric and dispersion interactions on the thermochemistry of crowded (fluoro)alkyl compounds. *Acc. Chem. Res.* **57**, 153–163 (2024).

16. Boehme, S. C. *et al.* Strongly Confined $CsPbBr_3$ Quantum Dots as Quantum Emitters and Building Blocks for Rhombic Superlattices. *ACS Nano* **17**, 2089–2100 (2023).

17. Malko, A. V. *et al.* Pump-intensity- and shell-thickness-dependent evolution of photoluminescence blinking in individual core/shell CdSe/CdS nanocrystals. *Nano Lett.* **11**, 5213–5218 (2011).

18. Puthenpurayil, J.; Cheng, O. H.-C.; Qiao, T.; Rossi, D.; Son, D. H. On the determination of absorption cross section of colloidal lead halide perovskite quantum dots. *J. Chem. Phys.* **151**, 154706 (2019).

19. Mi, C. *et al.* Biexciton-like Auger Blinking in Strongly Confined $CsPbBr_3$ Perovskite Quantum Dots. *J. Phys. Chem. Lett.* **14**, 5466–5474 (2023).

20. Nair, G.; Zhao, J.; Bawendi, M. G. Biexciton Quantum Yield of Single Semiconductor Nanocrystals from Photon Statistics. *Nano Lett.* **11**, 1136–1140 (2011).

21. Zhao, J.; Chen, O.; Strasfeld, D. B.; Bawendi, M. G. Biexciton Quantum Yield Heterogeneities in Single CdSe (CdS) Core (Shell) Nanocrystals and Its Correlation to Exciton Blinking. *Nano Lett.* **12**, 4477–4483 (2012).

22. Sercel, P. C. *et al.* Exciton Fine Structure in Perovskite Nanocrystals. *Nano Lett* **19**, 4068–4077 (2019).

23. Tamarat, P. *et al.* The ground exciton state of formamidinium lead bromide perovskite nanocrystals is a singlet dark state. *Nat. Mater.* **18**, 717–724 (2019).

24. Ji, Z.; Song, Z. Exciton radiative lifetime in CdSe quantum dots. *J. Semicond.* **44**, 032702–10 (2023).

25. Oriel, E. H. *et al.* Intraband Cooling and Auger Recombination in Weakly to Strongly Quantum-Confined CsPbBr3 Perovskite Nanocrystals. *J. Phys. Chem. Lett.* **15**, 6062–6068 (2024).

26. Rainò, G. *et al.* Underestimated effect of a polymer matrix on the light emission of single $CsPbBr_3$ nanocrystals. *Nano Lett.* **19**, 3648–3653 (2019).

27. Krieg, F. *et al.* Stable ultraconcentrated and ultradilute colloids of $CsPbX_3$ (X = Cl, Br) nanocrystals using natural lecithin as a capping ligand. *J. Am. Chem. Soc.* **141**, 19839–19849 (2019).

28. Zhu, C. *et al.* Room-temperature, highly pure single-photon sources from all-Inorganic lead halide perovskite quantum dots. *Nano Lett.* **22**, 3751–3760 (2022).

29. Li, B. *et al.* Excitons and biexciton dynamics in single $CsPbBr_3$ perovskite quantum dots. *J. Phys. Chem. Lett.* **9**, 6934–6940 (2018).

30. Makarov, N. S. *et al.* Spectral and Dynamical Properties of Single Excitons, Biexcitons, and Trions in Cesium–Lead-Halide Perovskite Quantum Dots. *Nano Lett.* **16**, 2349–2362 (2016).

31. Zhu, M.; Zhou, J.; Hu, Z.; Qin, H.; Peng, X. Effects of Local Dielectric Environment on Single-Molecule Spectroscopy of a CdSe/CdS Core/Shell Quantum Dot. *ACS Photonics* **5**, 4139–4146 (2018).

32. Senden, T.; Rabouw, F. T.; Meijerink, A. Photonic Effects on the Radiative Decay Rate and Luminescence Quantum Yield of Doped Nanocrystals. *ACS Nano* **9**, 1801–1808 (2015).

33. Utzat, H. *et al.* Probing linewidths and biexciton quantum yields of single cesium lead halide nanocrystals in solution. *Nano Lett.* **17**, 6838–6846 (2017).

34. Rainò, G. *et al.* Ultra-narrow room-temperature emission from single $CsPbBr_3$ perovskite quantum dots. *Nat. Commun.* **13**, 2587 (2022).

35. Morad, V. *et al.* Designer phospholipid capping ligands for soft metal halide nanocrystals. *Nature* **626**, 542–548 (2024).

36. Seth, S.; Ahmed, T.; Samanta, A. Photoluminescence Flickering and Blinking of Single CsPbBr3 Perovskite Nanocrystals: Revealing Explicit Carrier Recombination Dynamics. *J. Phys. Chem. Lett.* **9**, 7007–7014 (2018).

37. D'Amato, M. *et al.* Highly Photostable Zn-Treated Halide Perovskite Nanocrystals for Efficient Single Photon Generation. *Nano Lett.* **23**, 10228–10235 (2023).

38. Pierini, S. *et al.* Highly Photostable Perovskite Nanocubes: Toward Integrated Single Photon Sources Based on Tapered Nanofibers. *ACS Photonics* **7**, 2265–2272 (2020).

39. Hsu, B.-W. *et al.* Very Robust Spray-Synthesized CsPbI3 Quantum Emitters with Ultrahigh Room-Temperature Cavity-Free Brightness and Self-Healing Ability. *ACS Nano* **15**, 11358–11368 (2021).

40. Hu, F. *et al.* Slow Auger Recombination of Charged Excitons in Nonblinking Perovskite Nanocrystals without Spectral Diffusion. *Nano Lett.* **16**, 6425–6430 (2016).